$ZnFe_2O_4$ Leaves Grown on TiO_2 Trees Enhance Photoelectrochemical Water Splitting

*Xue-Li Zheng, Cao-Thang Dinh, F. Pelayo García de Arquer, Bo Zhang, Min Liu, Oleksandr Voznyy, Yi-Ying Li, Gordon Knight, Sjoerd Hoogland, Zheng-Hong Lu, Xi-Wen Du, and Edward H. Sargent**

***T**iO$_2$ has excellent electrochemical properties but limited solar photocatalytic performance in light of its large bandgap. One important class of visible-wavelength sensitizers of TiO_2 is based on $ZnFe_2O_4$, which has shown fully a doubling in performance relative to pure TiO_2. Prior efforts on this important front have relied on presynthesized nanoparticles of $ZnFe_2O_4$ adsorbed on a TiO_2 support; however, these have not yet achieved the full potential of this system since they do not provide a consistently maximized area of the charge-separating heterointerface per volume of sensitizing absorber. A novel atomic layer deposition (ALD)-enhanced synthesis of sensitizing $ZnFe_2O_4$ leaves grown on the trunks of TiO_2 trees is reported. These new materials exhibit fully a threefold enhancement in photoelectrochemical performance in water splitting compared to pristine TiO_2 under visible illumination. The new materials synthesis strategy relies first on the selective growth of FeOOH nanosheets, 2D structures that shoot off from the sides of the TiO_2 trees; these templates are then converted to $ZnFe_2O_4$ with the aid of a novel ALD step, a strategy that preserves morphology while adding the Zn cation to achieve enhanced optical absorption and optimize the heterointerface band alignment.*

X.-L. Zheng, Dr. C.-T. Dinh, Dr. F. P. G. de Arquer, Dr. B. Zhang, Dr. M. Liu, Dr. O. Voznyy, Dr. S. Hoogland, Prof. E. H. Sargent
Department of Electrical and Computer Engineering
University of Toronto
35 St George Street, Toronto, Ontario M5S 1A4, Canada
E-mail: ted.sargent@utoronto.ca

X.-L. Zheng, Prof. X.-W. Du
Institute of New-Energy Materials
School of Materials Science and Engineering
Tianjin University
Tianjin 300072, China

Y.-Y. Li, Prof. Z.-H. Lu
Department of Materials Science and Engineering
University of Toronto
184 College Street, Toronto, Ontario M5S 3E4, Canada

Dr. G. Knight
Trojan Technologies
3020 Gore Road London, Ontario N5V 4T7, Canada

DOI: 10.1002/smll.201600534

1. Introduction

Photoelectrochemical (PEC) processes offer a direct use of sunlight for a large variety of applications, including hydrogen production for energy storage, as well as hydroxyl radical formation for pollutant degradation.[1,2] Among the various photocatalysts developed to date, TiO_2 is particularly suited to commercial scale-up because it is abundant, nontoxic, and stable under photochemical conditions.[3–6] Unfortunately, its large bandgap limits its photoactivity to the ultraviolet (UV) region. As a result, in the best case it can absorb only up to 5% of incident solar photons. This limits its potential to increase further in photoelectrochemical efficiency.

Strategies to expand the TiO_2 optical absorption spectrum into the visible region include the sensitization of TiO_2 with dyes or small-bandgap semiconductors,[7–9] doping,[10–13] and coupling TiO_2 with plasmonic nanostructures.[14–17] The synergistic effects of coupling TiO_2 with another

semiconductor include the enhancement of charge separation, visible light absorption, and photostability. Each of these properties is important for practical use in environmental applications.[13,18–20] For these reasons, a variety of semiconductors such as metal oxides, metal sulfides, and metal or carbon nitrides have been used to improve the activity of TiO_2 in the visible region.[21–25]

We took the view that the synergistic combination of TiO_2 with spinel $ZnFe_2O_4$ stands to augment photocatalytic performance considerably. Spinel $ZnFe_2O_4$ is a semiconductor with a bandgap of 1.9 eV that forms a type II heterostructure with TiO_2.[26,27] It has better photochemical stability compared to other small-bandgap materials such as metal sulfides and selenides. Several approaches have been employed to synthesize $ZnFe_2O_4/TiO_2$ (ZFO/TiO_2) heterostructures, including electrochemical, hydrothermal, and plasma spray methods.[26,28,29] These heterostructures exhibit increased photoelectrochemical performance compared to pristine TiO_2 electrodes.

Prior attempts have unfortunately provided limited efficiency gains. We hypothesized that the issue was an architectural one: forming of $ZnFe_2O_4$ nanoparticles on TiO_2 surface failed to offer the kinds of interfacial areas, and intimate chemical contact between the two constituent materials, required to form efficient heterojunctions.[26–31] Nanoparticle-covered 1D structures exhibit relatively low multiples of sensitization, as well as suffering from a small reaction area and limited capacity for reagent diffusion for photoelectrochemical reactions.

In seeking an improved architecture, we turned to the structure of plants such as corn and sugarcane – efficient systems for the conversion of solar energy to fuels. Plants begin with 1D trunks that branch into 2D leaves that facilitate sunlight absorption. The role of the 1D portion is to improve the mass transport while the 2D is a surface-area maximizing strategy that facilitates sunlight absorption, photosynthetic reaction area, and the diffusion of reactants.[32,33]

We reasoned that TiO_2 (1D) TiO_2 nanowires (NWs), already available thanks to multiple prior advances,[34–38] could be used as a template on top of which to grow heterostructures based on multimetal oxide nanosheets.

Unfortunately, we found that anisotropic 2D shapes are often unstable at the high temperatures, while high temperature is normally required to form a crystalline phase of mixed oxides.[39] This incompatibility make it challenging to grow 2D shaped multimetal oxide materials.

We report herein a new synthetic route that allows the construction of $ZnFe_2O_4$ nanosheets on TiO_2 templates. Specifically, the $ZnFe_2O_4/TiO_2$ heterostructures are constructed using a combination of solution-phase materials growth techniques and completed with a final atomic layer deposition (ALD) step. The templated growth begins with the realization of FeOOH nanosheets on the surface of TiO_2 nanowires. These we then convert into $ZnFe_2O_4$ via an ensuing coating of ZnO grown by atomic ALD.

We find that the new heterostructures exhibit photoelectrochemical water splitting performance that is fully 3× higher than relevant controls under visible illumination. These results demonstrate that control over multistep multimaterial nanostructuring can enhance photoelectrochemical water splitting under sunlight.

2. Results and Discussion

2.1. Synthesis and Characterization of ZFO/TiO_2 Controlling the Growth of ZFO on TiO_2 NW

The hierarchical $ZnFe_2O_4$ nanosheet/TiO_2 nanowire structures were synthesized via a two-step approach. First, FeOOH nanosheets templates are obtained via a solution-based 2D crystal growth method. We then use atomic layer deposition of a ZnO surface layer (**Figure 1**A) for conversion.

In detail, TiO_2 nanowire arrays were synthesized on fluorine-doped tin oxide (FTO) glass substrate by a hydrothermal method.[40] TiO_2 nanowire arrays were rinsed with 5×10^{-3} M $FeCl_3$ solution. After 120 min sonication treatment, the shell layers have a nanosheet structure rather than being a continuous thin film shell on the surface of TiO_2 nanowire arrays (Figure S1, Supporting Information). These nanosheets are FeOOH per prior reports.[41] The distribution of the shell nanosheets is tuned by controlling the Fe^{3+} treatment time (Figure S2, Supporting Information). Subsequent to the nanosheet formation, a conformal layer of ZnO was deposited on $FeOOH/TiO_2$ heterostructures using an atomic layer deposition process. Finally, $ZnFe_2O_4/TiO_2$ heterostructures were obtained by 520 °C thermal treatment and 5 M KOH immersion to remove excess ZnO (Figure S6, Supporting Information).

The morphologies of pristine TiO_2 nanowire arrays and ZFO/TiO_2 heterostructures were characterized using scanning electron microscopy (SEM). The nanowires are tetragonal in shape with square top facets and an average diameter of 30 nm (Figure 1B). Cross-sectional SEM image (Figure S3, Supporting Information) shows that pristine TiO_2 nanowire film consists of dense and vertically aligned nanowire arrays with a length of ≈5 μm. The SEM images of $FeOOH/TiO_2$ and ZFO/TiO_2 heterostructures are shown in Figure 1C,D. The film structure remains uniform over a large area, indicating that the nanowire arrays are intact during the growth of $ZnFe_2O_4$ (Figure S1B, Supporting Information). High-magnification SEM images (Figure 1E) show that TiO_2 nanowire arrays were uniformly covered with $ZnFe_2O_4$ nanosheets, forming TiO_2-$ZnFe_2O_4$ core–shell structures on the nanowires with the $ZnFe_2O_4$ shell having a thickness of 30–50 nm (Figure 1E). To examine the crystalline structure of $ZnFe_2O_4$ and TiO_2, we used high resolution transmission electron microscope (HR-TEM). TiO_2 nanowires are single-crystalline with [001] orientation (Figure 1F). The observed lattice spacing of 0.32 nm belongs to the [110] interplanar distance of rutile TiO_2. In addition to the pristine TiO_2, a crystalline structure with the lattice fringes of 0.29 nm is also present (Figure 1G), which matches well with the [220] crystallographic plane of spinel $ZnFe_2O_4$.

To verify the crystal structure of ZFO/TiO_2 heterostructures, we used X-ray diffraction (XRD), which reveals

DOI: 10.1002/smll.201600534

small NANO MICRO

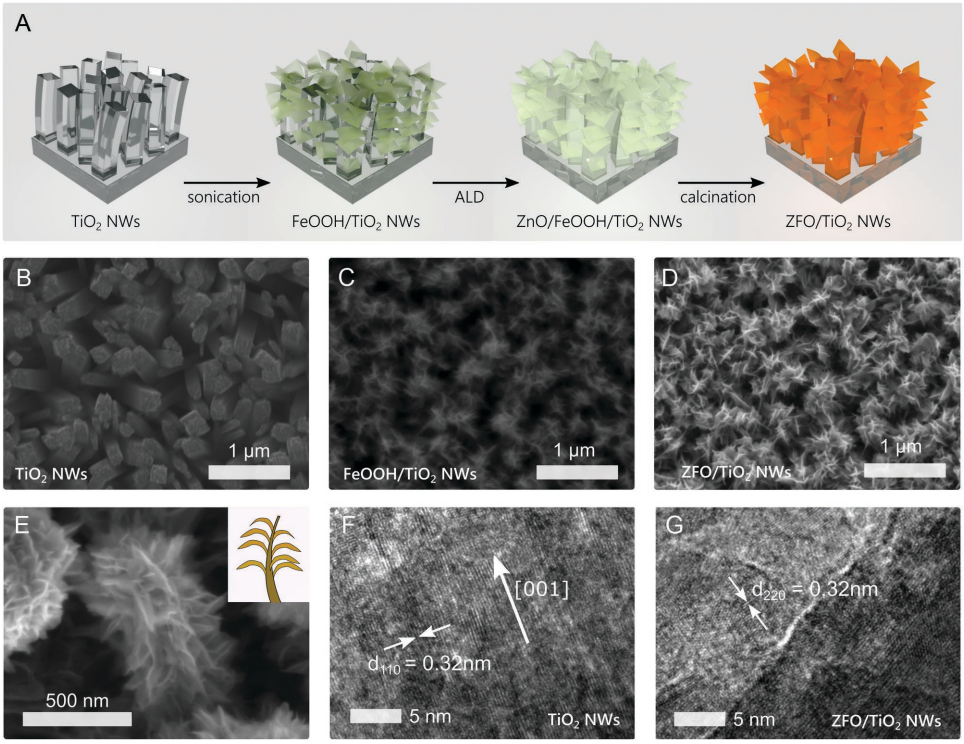

Figure 1. Preparation and morphology characterization of ZFO/TiO_2 heterostructures. A) Schematic illustration of the multiple steps of the preparation of ZFO/TiO_2. Top-surface SEM images of B) TiO_2 NWs, C) FeOOH/TiO_2 NWs, and D) ZFO/TiO_2 NWs. E) Closer SEM view of a typical ZFO/TiO_2 NW tree and its resemblance with the structure of a corn tree (inset). HRTEM images of F) TiO_2 nanowire arrays and G) ZFO/TiO_2 heterostructures.

that (**Figure 2**A) TiO_2 nanowire arrays have well-defined diffraction peaks typical of highly crystalline rutile TiO_2 (JCPDS 88-1175). In the XRD pattern of ZFO/TiO_2 heterostructures, an additional diffraction peak is present at $2\theta = 30.48°$, which we attribute to the (220) hkl plane of the $ZnFe_2O_4$ crystal structure.

To investigate the oxidation states of the metal and the surface composition in ZFO/TiO_2 heterostructures, we employed X-ray photoelectron spectroscopy (XPS) (Figure 2B). Two peaks in the Ti 2p XPS spectrum are present at the binding energies of 464.8 and 459.2 eV. These binding energies are in good agreement with those of Ti^{4+} oxidation states in pristine rutile TiO_2.[42] Compared those in pristine TiO_2 nanowires, the Ti 2p peaks become much weaker in the XPS spectrum of ZFO/TiO_2 heterostructures. This result further confirms that in the ZFO/TiO_2 heterostructures, $ZnFe_2O_4$ nanosheets cover the surface of the TiO_2 nanowires.

Figure 2C,D shows the Zn 2p and Fe 2p XPS spectra of Zn and Fe in ZFO/TiO_2 heterostructures, respectively. The two peaks appeared in the Zn 2p XPS spectra (Figure 2C) at the binding energies of 1044.4 and 1022.8 eV are characteristics of Zn 2p1/2 and Zn 2p3/2, respectively.[43] This reveals the oxidation state of Zn^{2+} in the heterostructures. In the case of Fe 2p, the two peaks located at 710.6 and 724.4 eV should be assigned to the spectra of Fe 2p3/2 and Fe 2p1/2 for Fe^{3+}.[44] The Zn/Fe atomic ratio, calculated from XPS spectra is 1:2, which matches well with that in $ZnFe_2O_4$ material. The combination of the oxidation states and the atomic ratios confirms the presence of highly stoichiometric $ZnFe_2O_4$ material in the devices.

2.2. Controlling the Growth of ZFO on TiO_2 NW

To control the growth of ZFO on TiO_2, we systematically modified the FeOOH template by varying the treatment time of TiO_2 NW arrays in the Fe^{3+} solution. As shown in **Figure 3**A, the color of ZFO/TiO_2 samples changes from light yellow to red orange when the treatment time increases from 60 to 180 min. This indicates that the amount of $ZnFe_2O_4$ loaded on ZFO/TiO_2 heterostructures increases with longer treatment time, which is confirmed by UV–vis absorption spectroscopy (Figure 3B). The absorption band at 600 nm, characteristic of $ZnFe_2O_4$ with a band gap of 2.1 eV, is also intensified with increasing treatment time, indicative of higher $ZnFe_2O_4$ content.

We then monitored the change in morphology of ZFO/TiO_2 heterostructures with different Fe^{3+} treatment times (Figure 3C). Only a small amount of $ZnFe_2O_4$ is observed on the surface of TiO_2 NWs with 60 min of treatment. Extending the treatment time to 120 min resulted in large $ZnFe_2O_4$ nanosheets growing on the surface of TiO_2 NWs (Figure 1C,D). The slow growth rate of the nanosheets suggests that the growth of $ZnFe_2O_4$ stem directly from the TiO_2 NW surface. We propose that the higher potential energy barrier originates from the lattice mismatch between TiO_2 and $ZnFe_2O_4$ crystallites and results in slower growth kinetics of $ZnFe_2O_4$. After 180 min of Fe^{3+} treatment, the NWs become surrounded by nanosheets as observed in Figure 3D. Blade-like $ZnFe_2O_4$ nanosheets emerge from the center of original TiO_2 NWs. $ZnFe_2O_4$ nucleates on preexisting nanosheets

DOI: 10.1002/smll.201600534

www.MaterialsViews.com

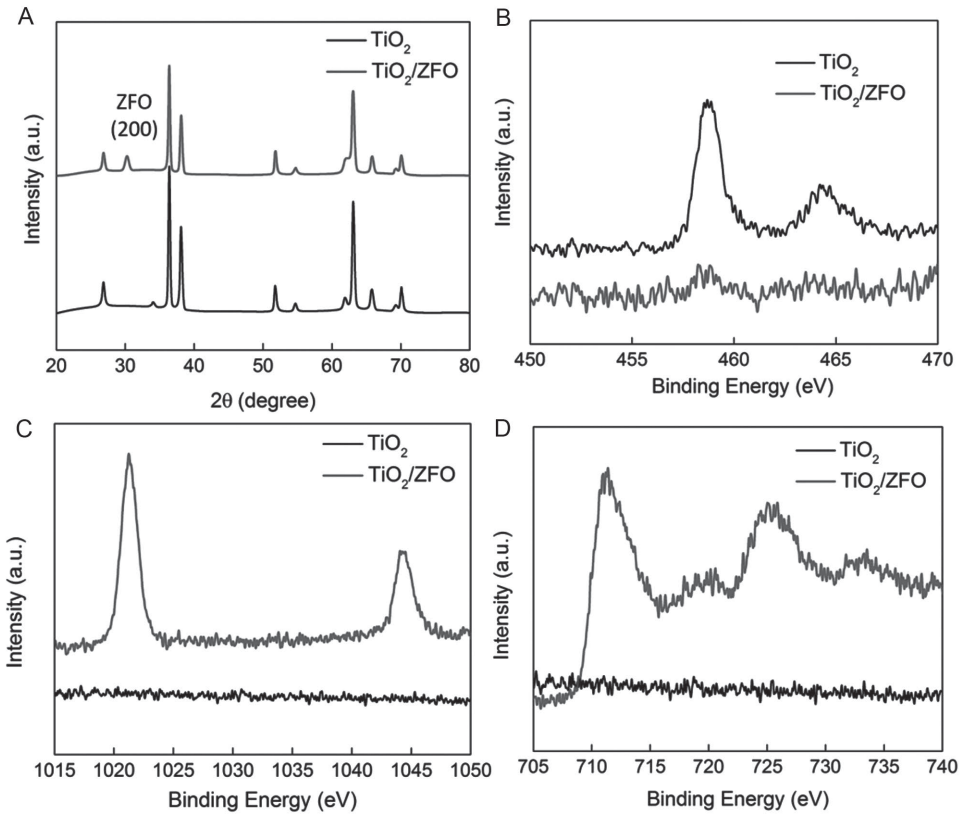

Figure 2. Crystallized structure and valence state of ZFO/TiO_2 heterostructures. A) XRD patterns of TiO_2 NWs (lower line) and $ZnFe_2O_4$ nanosheets/TiO_2 NWs (upper line) heterostructures. B) Ti 2p XPS spectra (TiO^2 upper line), C) Zn 2p XPS spectra (TiO^2 lower line), and D) Fe 2p XPS spectra of the TiO_2 NWs (TiO^2 lower line) and $ZnFe_2O_4$ nanosheets/TiO_2 NWs heterostructures.

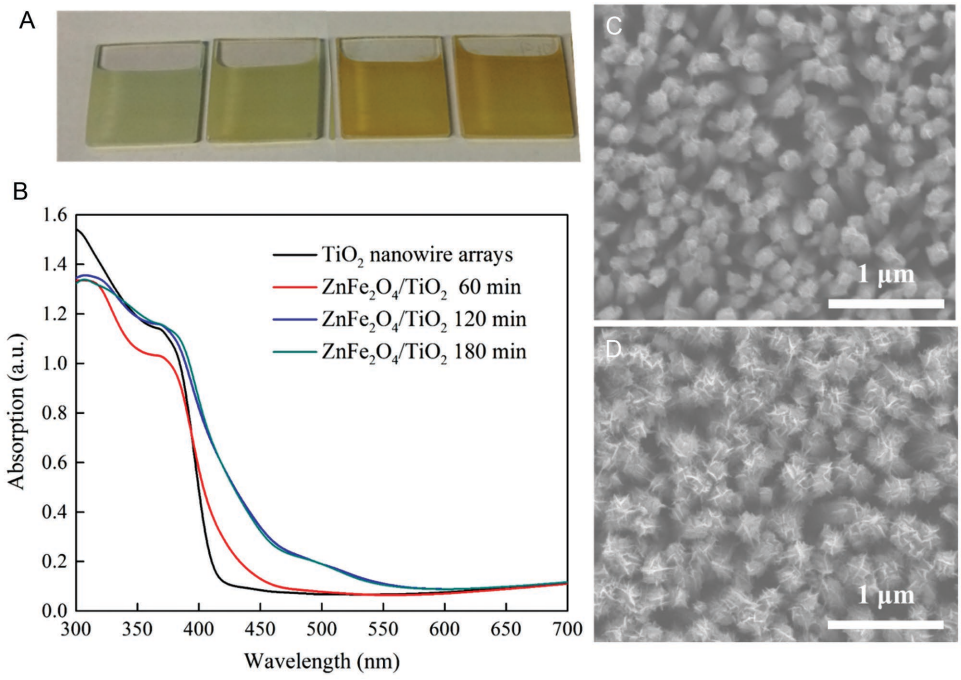

Figure 3. Characterization of ZFO/TiO_2 varying time. A) Photographs and B) UV–vis spectrum of the ZFO/TiO_2 heterostructures with varying Fe^{3+} treatment time. SEM images of $ZnFe_2O_4$/TiO_2 heterostructures with Fe^{3+} treatment C) 60 min and D) 180 min, respectively.

small 2016,
DOI: 10.1002/smll.201600534

that, with a lower energy barrier and better epitaxy, would yield a faster reaction rate.

2.3. Photoelectrochemical Performance of TiO_2 Hybrids

To study the PEC performance of ZFO/TiO_2 heterostructures with different ZFO loadings and of pristine TiO_2 NW for water splitting, the samples were fabricated as photoanodes with a well-defined area of 1 cm^2. All PEC measurements were performed in a standard three-electrode electrochemical cell with a Pt wire as the counter electrode, an Ag/AgCl reference electrode, and 1 M KOH as the electrolyte solution. The reversible hydrogen electrode (RHE) potential was converted from the Ag/AgCl reference electrode as RHE = V(Ag/AgCl) + 1.0 V. Linear sweeps in a potential window between 0.2 and 1.8 V versus RHE collected for ZFO/TiO_2 heterostructures and pristine TiO_2 NW under simulated sunlight illumination at 100 mW cm^{-2} is shown in **Figure 4**A. The pristine TiO_2 nanowire arrays exhibit a photocurrent density of 0.5 mA cm^{-2} at 1.0 V versus RHE. Coupling TiO_2 NWs with $ZnFe_2O_4$ increases the current density of TiO_2 NWs (Figure 4A). It also can be concluded that the series resistance is lower for $ZnFe_2O_4$ samples while the shunt resistance remains unmodified from a function of applied potential versus RHE.

In order to investigate any benefits derived from the nanosheet structure, we synthesized ZFO/TiO_2 heterostructures in which $ZnFe_2O_4$ nanoparticles are grown on TiO_2 NWs nanoparticles (Figure S5, Supporting Information). As shown in Figure 4A, both $ZnFe_2O_4$ nanoparticles and $ZnFe_2O_4$ nanosheets on TiO_2 NWs heterostructures show increased photocurrent density compared to pristine TiO_2 NW arrays at 1.0 V versus RHE. The highest current density is obtained with ZFO/TiO_2 heterostructures with 120 min of sonication treatment, reaching a current density of 0.7 mA cm^{-2} at 1.0 V versus RHE, which is 1.4 times higher than that of pristine TiO_2 NWs and 1.2 times higher than that of ZFO nanoparticles/TiO_2 heterostructures. Increasing the treatment time further decreases the performance of ZFO/TiO_2

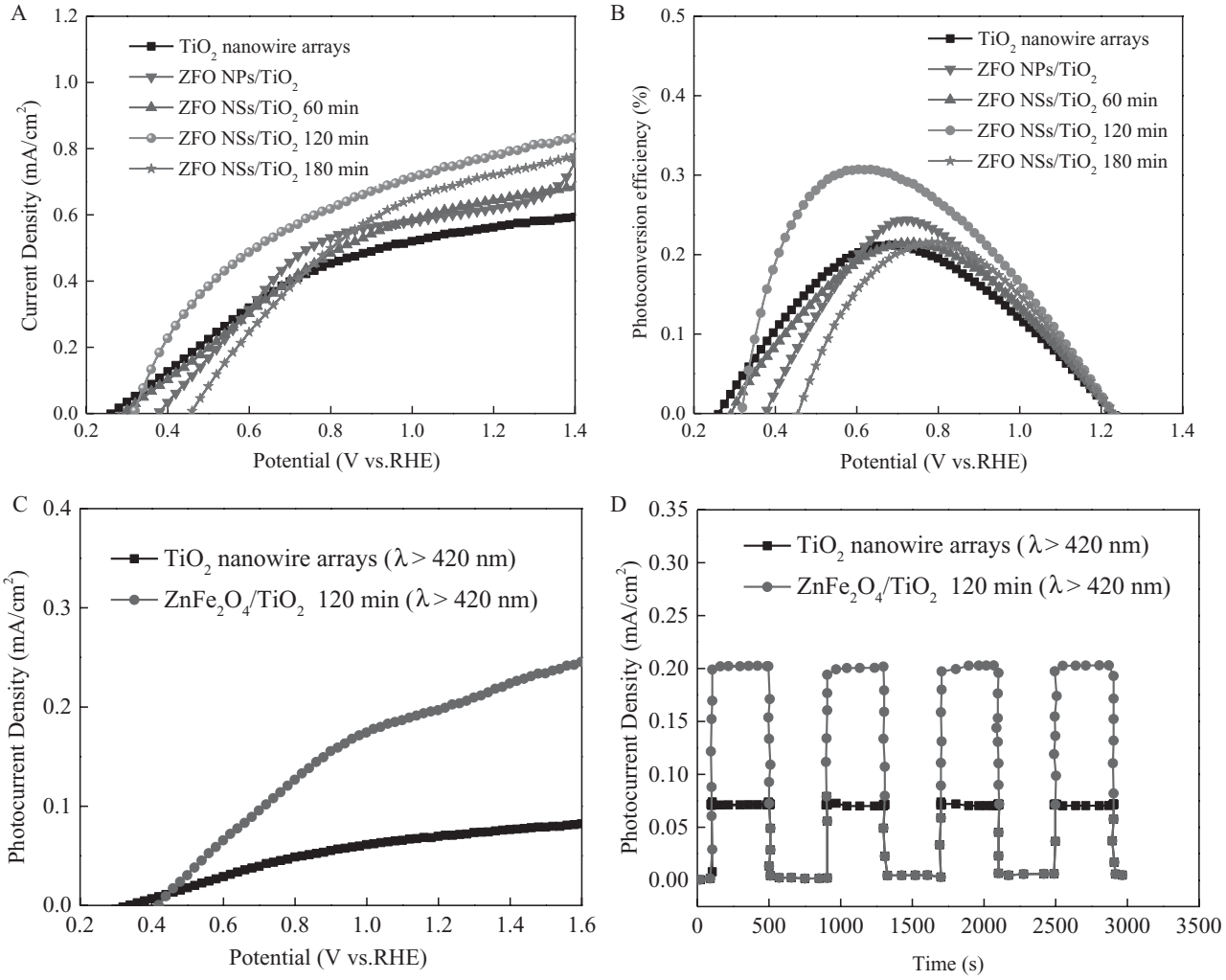

Figure 4. Performance comparison of ZFO/TiO_2 heterostructures and pristine TiO_2 NWs. A) Variation of photocurrent density and B) photoconversion efficiency versus bias potential (vs RHE) under solar illumination (100 mA cm^{-2}). C) Variation of photocurrent density versus bias potential (vs RHE) under visible light irradiation ($\lambda > 420$ nm). D) Time-dependent photocurrent density of TiO_2 NW and ZFO/TiO_2 heterostructure photoanode at repeated on/off cycles of visible light illumination.

DOI: 10.1002/smll.201600534

heterostructures. Longer treatment time may result in an increase of ZFO size but a constant interface area between ZFO and TiO_2 NWs. The larger size of ZFO may induce charge recombination due to the short diffusion length of ZFO,[45] leading to a decrease in performance. The amount of $ZnFe_2O_4$ loaded on TiO_2 affects the onset potentials of resulting $ZnFe_2O_4/TiO_2$ heterostructures. With increasing amount of $ZnFe_2O_4$ nanosheets on TiO_2, the onset potential is shifted to more positive potentials. This effect could be explained by the change in conduction band of $ZnFe_2O_4/TiO_2$ heterostructures with varying $ZnFe_2O_4$ amount. In addition, the amount of $ZnFe_2O_4$ also affects the coverage of TiO_2 nanowire surface which changes the surface activity of the heterostructure in water oxidation. This could also lead to the change in onset potential of the heterostructures.

The photoconversion efficiency η is obtained from

$$\eta(\%) = J_P\left[(1.23 - V_{app})/I_0\right] \quad (1)$$

where J_p is the photocurrent density (mA cm^{-2}), I_0 is the intensity of incident light (mW cm^{-2}), and V_{app} is the applied potential to the photoanode (V versus RHE). Figure 4B shows the total percent photoconversion efficiency η (%) as a function of applied potential (E_{app} vs RHE) for the ZFO/TiO_2 heterostructures and pristine TiO_2 nanowire arrays under AM 1.5. A maximum photoconversion efficiency of 0.31% is obtained at an applied potential of 0.60 V versus RHE for the ZFO/TiO_2 heterostructures, while it was 0.21% for pristine TiO_2 nanowire arrays at 0.65 V versus RHE. The overall solar to hydrogen conversion efficiency is dependent not only on the light absorption and charge separation efficiency, but also on the catalytic activity of the electrodes. In this case, the catalytic activity of water oxidation on $ZnFe_2O_4$ limit the overall water splitting efficiency. This could be enhanced by coupling the photoanode heterostructure with superior water oxidation catalyst.

We then sought to investigate the effect of ZFO loading on the photoelectrochemical performance of TiO_2 NWs under visible light irradiation by applying a 420 nm cut-off filter to remove the fraction of the UV light of the simulated solar spectrum. The data (Figure 4C) reveal that ZFO/TiO_2 shows a much higher performance compared to pristine TiO_2 NWs under visible light illumination. At 1.0 V versus RHE, ZFO/TiO_2 heterostructures exhibit a current density of 0.18 mA cm^{-2}. This value is fully three times higher than that of pristine TiO_2 NWs (0.06 mA cm^{-2}). The photocurrent on ZFO/TiO_2 under 1.5 AM solar obtained with back side illumination is slightly higher than that obtained with front side illumination. This result could be explained by the fact that the TiO_2 is the main contribution to the photocurrent density of ZFO/TiO_2 heterostructures. The ZFO on the top of TiO_2 NW array could reflect the UV light when illuminating from the front, leading to a slight decrease in overall performance of ZFO/TiO_2.

To study the chemical and structural stability during PEC water splitting, we carried out time-dependent measurement on ZFO/TiO_2 heterostructures and TiO_2 NWs as shown in Figure 4D. The rise and fall of the photocurrent corresponded well to the illumination being switched on and off. When the illumination was interrupted, the current rapidly dropped to almost zero. Upon illumination, the photocurrent reverted to the original steady state value within a couple of seconds (>90% of the steady state value was obtained instantaneously). The ZFO/TiO_2 heterostructures show a highly stable photocurrent density of ≈0.2 mA cm^{-2} versus 1.2 V RHE with repeated on/off cycles under visible light over the course of 3000 s. This result implies that the formation of a heterojunction between ZFO and TiO_2 increases the separation of photogenerated holes and electrons which prolong the lifetime of generated charges, leading to a higher photoelectrocatalytic activity compared to pristine TiO_2 nanowires. These data suggest that with the high activity and potential long-term stability, ZFO/TiO_2 heterostructures could be ideal for visible light driven photoelectrocatalysis.

The mechanism for the enhancement in PEC performance of ZFO/TiO_2 heterostructures compared to TiO_2 NWs is illustrated in **Figure 5**. Ultraviolet photoelectron spectroscopy (UPS) indicates the work function and valence band maximum level of TiO_2 and $ZnFe_2O_4$, confirming a type II band alignment in $TiO_2/ZnFe_2O_4$ heterostructures (Figure 5A,B). The overall conversion process is depicted as follows: ZFO is excited by incident light and generates electron–hole pairs (step 1), and electrons in the conduction band of $ZnFe_2O_4$ are transferred to conductive FTO though TiO_2 NWs (step 2). At the same time, the holes in the valence band of $ZnFe_2O_4$ oxidize H_2O to O_2 (step 3). The charge separation between TiO_2 NWs and $ZnFe_2O_4$ enhances photoelectrochemical performance under solar and visible light illumination. 2D $ZnFe_2O_4$ with large surface area exposed also contribute to performance of ZFO/TiO_2 heterostructures.

3. Conclusion

We report herein a sequential pathway to the materials synthesis of 2D/1D multimetal oxide nanosheets/TiO_2 nanowire heterostructures. We achieved this by depositing the nanosheets with a mixture of metal oxide precursors using a solution phase method followed by an ALD-based cation introduction. We demonstrate an application of these new materials enabled by growing $ZnFe_2O_4/TiO_2$ heterostructures involving an initial growth of FeOOH nanosheets template on TiO_2 NWs, which we subsequently convert into $ZnFe_2O_4$ by ZnO ALD deposition and thermal treatment. Our 2D/1D $ZnFe_2O_4/TiO_2$ heterojunctions exhibit 1.4 and three times higher photoelectrochemical performance compared to that of pristine TiO_2 NWs under solar and visible light illumination, respectively. The 2D/1D $ZnFe_2O_4/TiO_2$ heterostructures form a material system that enhances photoelectrochemical water splitting. The strategy may be extended to other mixed-metal oxide nanosheets systems having applications in catalysis, energy storage, and conversion.

4. Experimental Section

Materials: Iron (III) chloride ($FeCl_3$) and titanium isopropoxide (99% Aldrich) were purchased from Sigma-Aldrich. All the chemicals were used without further purification.

small 2016,
DOI: 10.1002/smll.201600534

small NANO MICRO

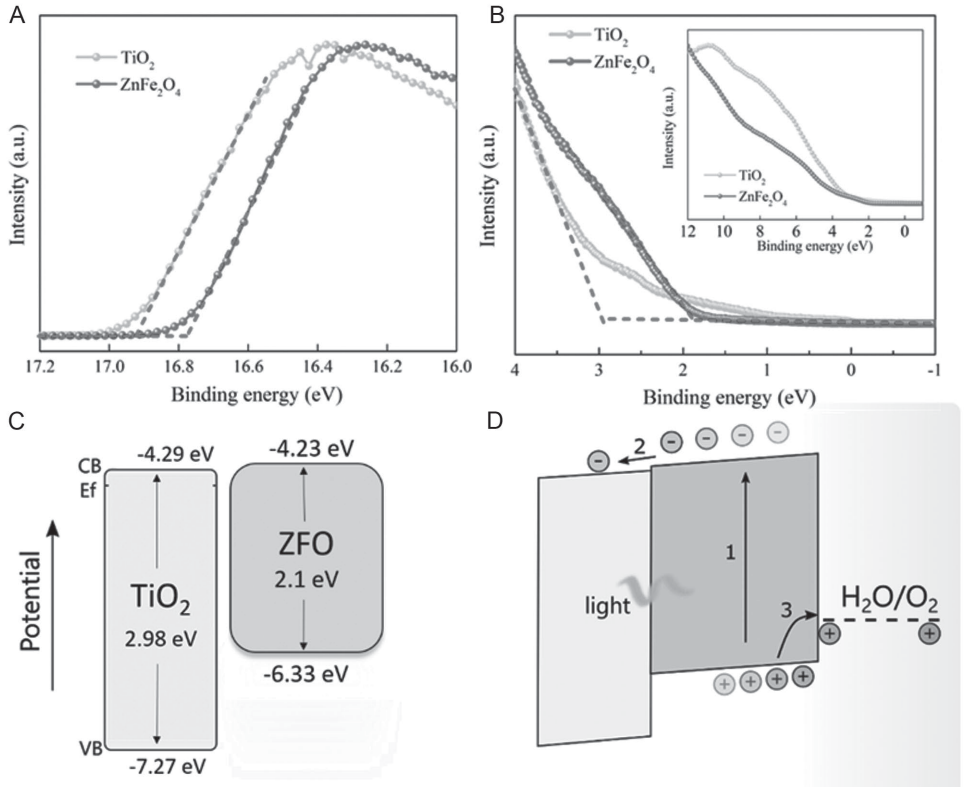

Figure 5. UPS spectra of pure TiO_2 and $ZnFe_2O_4$ and energy level diagram of the ZFO/TiO_2 heterostructure. A) A detailed spectrum of inelastic cutoff region. It also shows the cutoff energy with a vertical bar. B) Fermi edge region, which is similar to (A). C,D) Energy level diagram of ZFO/TiO_2 before and after contact, respectively. (1) Visible light is absorbed in the ZFO phase. Photogenerated charges are split via drift or diffusion. (2) Electrons get injected into the TiO_2 phase to then recirculate through the external driving circuit. (3) Holes remain at the ZFO to oxidize water. On top of the structural benefit, the heterostructure architecture reduces electron–hole recombination in the ZFO therefore increasing the yield of the reaction.[31]

Synthesis of TiO_2 Nanowire Arrays on FTO Substrate: In a typical process, the FTO substrates were first cleaned with a mixture of isopropanol and water for 2 h under sonication condition and were then dried with N_2 gas at room temperature. To a mixture of deionized water (15 mL) and hydrochloric acid (15 mL, 36.5 wt%), was added titanium isopropoxide (0.45 mL, 99% Aldrich) under stirring condition. After 1 h of stirring, the mixture was transferred to a Teflon-lined stainless steel autoclave. Cleaned FTO/glass substrates (2 cm × 2 cm) were immersed into the water/HCl/titanium isopropoxide mixture with the conducting side face down. The autoclave was put in an oven set at a temperature of 160 °C and was taken out from the oven after 5 h of crystallization. The autoclave was cooled down to room temperature and the TiO_2 NWs grown on FTO substrate were washed several time with ethanol and DI water and were subsequently annealed at 450 °C in air for 1 h.

Synthesis of 2D/1D $ZnFe_2O_4$ Nanosheets/TiO_2 Nanowires Heterostructures: The annealed TiO_2 nanowire arrays substrate were immersed into 5×10^{-3} M $FeCl_3$ aqueous solution. The mixture was then sonicated for different time. The obtained FeOOH/TiO_2 composite were cleaned with isopropyl alcohol and DI water followed by a drying step with N_2 gas. ZnO layer was deposited on the surface of FeOOH/TiO_2 by ALD technique using diethylzinc (99.90%, Strem) and pure DI water as the precursors. 50 cycles of ALD were used to produce ZnO layer with a thickness of 10 nm. Finally, $ZnFe_2O_4$/TiO_2 heterostructures were obtained by annealing ZnO/FeOOH/TiO_2 at 520 °C for 3 h followed by a treatment with 5 M KOH solution to remove excess ZnO.

Characterization: Surface SEM and cross-section SEM of TiO_2 nanowires and $ZnFe_2O4$/TiO_2 heterostructures were taken on a Hitachi SU8230 scanning electron microscope operated at 1.0 kV. Transmission electron microscopy (TEM) and HRTEM images of the samples were taken on a Hitachi HF3300 transmission electron microscope operated at 300 kV. The samples were prepared on carbon-coated copper TEM grids (Ted Pella, Redding, CA) using micropipettes and were dried under ambient condition. Powder XRD patterns were obtained with MiniFlex600 instrument. Data was collected in Bragg-Brettano mode using 0.02° divergence with a scan rate of 0.1° s^{-1}. XPS measurements were carried out in a Thermo Scientific K-Alpha system, with a 300 μm spot size, 75 eV pass energy, and energy steps of 0.05 eV, aluminum anode X-ray excitation. UPS spectra were performed in a PHI5500 Multi-Technique system using nonmonochromatized He-Iα radiation (UPS, $h\nu$ = 21.22 eV). All work function and valence band measurements were performed at a take-off angle of 88°, and the chamber pressure was ≈10–9 torr. Work functions (WF) were calculated from the secondary electron cut-off (SEC) using the equation WF = 21.22 eV − SEC. The differences between Fermi levels and valence band maximum, η, were determined from the low binding energy onset. The absorbance of the samples has been obtained using an integrating sphere attachment in a PerkinElmer Lambda900 spectrophotometer to avoid scattering and reflectance. The generation of O_2 during the water splitting has been examined by gas chromatography (PerkinElmer Clarus 680) equipped with Molecular sieve 5A capillary column and thermal conductivity detector (Figure S8, Supporting Information).

DOI: 10.1002/smll.201600534

Photoelectrochemical Measurement: Photoelectrochemical measurements were performed using a three-electrode system connected to an electrochemical workstation (Autolab PGSTAT302N) in 1 M KOH electrolyte. $ZnFe_2O_4/TiO_2$ electrode were used as the working electrode (photoanode). Ag/AgCl (saturated KCl) electrode and Pt wire were used as reference electrode and counter electrode, respectively. Photocurrent versus voltage (*I–V*) characteristics were recorded from –1 V to +1 V with a scan rate of 1 mV s^{-1}. All experiments were performed at ambient temperature (22 °C ± 2 °C) and electrode potentials were converted to the RHE scale using $E(\text{RHE}) = E(\text{Ag/AgCl}) + 0.197\ \text{V} + 0.059 \times \text{pH}$. Where *E*(RHE) is the converted potential versus RHE, and *E*(Ag/AgCl) is the measured potential versus Ag/AgCl reference electrode. Transient photocurrent density versus time plots of TiO_2 and $ZnFe_2O_4/TiO_2$ heterostructures were recorded at an applied potential of 1.2 V versus RHE under visible light sources.

Supporting Information

Supporting Information is available from the Wiley Online Library or from the author.

Acknowledgements

X.-L.Z. and C.-T.D. contributed equally to this work. This work was financially supported by the Ontario Research Fund – Research Excellence Program and the Natural Sciences and Engineering Research Council (NSERC) of Canada. X.-L.Z. acknowledges a scholarship from the China Scholarship Council (CSC) (20140625004). This work was also supported by the National Basic Research Program of China (#2014CB931703) and the Natural Science Foundation of China (#51571149). The authors thank Y. J. Pang, M. X. Liu, and L. N. Quan for fruitful discussions; R. Wolowiec and D. Kopilovic for their help during the course of study; Y. Gong of Trojan Technologies for laboratory assistance.

[1] A. Fujishima, K. Honda, *Nature* **1972**, *238*, 37.
[2] X. Chen, S. Shen, L. Guo, *Chem. Rev.* **2010**, *110*, 6503.
[3] H. G. Yang, C. H. Sun, S. Z. Qiao, *Nature* **2008**, *453*, 638.
[4] C. T. Dinh, T. D. Nguyen, F. Kleitz, *ACS Nano* **2009**, *3*, 3737.
[5] M. R. Hoffmann, S. T. Martin, W. Choi, *Chem. Rev.* **1995**, *95*, 69.
[6] X. Chen, S. S. Mao, *Chem. Rev.* **2007**, *107*, 2891.
[7] B. O'Regan, M. Grätzel, *Nature* **1991**, *353*, 737.
[8] S. C. Hayden, N. K. Allam, M A. El-Sayed, *J. Am. Chem. Soc.* **2010**, *132*, 14406.
[9] J. Ryu, S. H. Lee, D. H. Nam, *Adv. Mater.* **2011**, *23*, 1883.
[10] R. Asahi, T. Morikawa, T. Ohwaki, *Science* **2001**, *293*, 269.
[11] S. U. M. Khan, Al-M. Shahry, W B. Ingler, *Science* **2002**, *297*, 2243.
[12] S. Hoang, S. Guo, N. T. Hahn, *Nano Lett.* **2011**, *12*, 26.
[13] X. Chen, L. Liu, Y. Y. Peter, S.S. Mao, *Science* **2011**, *331*, 746.
[14] Y. Tian, T. Tatsuma, *J. Am. Chem. Soc.* **2005**, *127*, 7632.
[15] S. Linic, P. Christopher, D. B. Ingram, *Nat. Mater.* **2011**, *10*, 911.
[16] Q. Zhang, D. Q. Lima, I. Lee, *Angew. Chem.* **2011**, *123*, 7226.
[17] L. Liu, S. Ouyang, J. Ye, *Angew. Chem.* **2013**, *125*, 6821.
[18] F. X. Xiao, J. Miao, H. B. Tao, *Small* **2015**, *11*, 2115.
[19] Y. C. Pu, G. Wang, K. D. Chang, *Nano Lett.* **2013**, *13*, 3817.
[20] H. Wang, L. Zhang, Z. Chen, *Chem. Soc. Rev.* **2014**, *43*, 5234.
[21] J. Tian, Z. Zhao, A. Kumar, *Chem. Soc. Rev.* **2014**, *43*, 6920.
[22] S. Liu, Z. R. Tang, Y. Sun, *Chem. Soc. Rev.* **2015**, *44*, 5053.
[23] M. Stefik, M. Cornuz, N. Mathews, T. Hisatomi, S. Mhaisalkar, M. Grätzel, *Nano Lett.* **2012**, *12*, 5431.
[24] X.-L. Zheng, W.-J. Qin, T. Ling, C.-F. Pan, X.-W. Du, *Adv. Mater. Interfaces* **2015**, *2*, 1400464.
[25] Y. Zhang, S. Jiang, W. Song, P. Zhou, H. Ji, W. Ma, W. Hao, Ch Chen, J. Zhao, *Energy Environ. Sci.* **2015**, *8*, 1231.
[26] Y. Hou, X.-Y. Li, Q.-D. Zhao, X. Quan, G.-H. Chen, *Adv. Funct. Mater.* **2010**, *20*, 2165.
[27] X. Li, Y. Hou, Q. Zhao, G. Chen, *Langmuir* **2011**, *27*, 3113.
[28] M. Wang, L. Sun, J. Cai, P. Huang, Y. Su, C. Lin, *J. Mater. Chem. A* **2013**, *1*, 12082.
[29] D. Hong, Y. Yamada, M. Sheehan, S. Shikano, C.-H. Kuo, M. Tian, C.-K. Tsung, S. Fukuzumi, *ACS Sus. Chem. Eng.* **2014**, *2*, 2588.
[30] P. Guo, L. Cui, Y. Wang, M. Lv, B. Wang, X. S. Zhao, *Langmuir* **2013**, *29*, 8997.
[31] K. J. McDonald, K.-S. Choi, *Chem. Mater.* **2011**, *23*, 4863.
[32] H. Zhou, X. Li, T. Fan, *Adv. Mater.* **2010**, *22*, 951.
[33] E. Shimoni, R.H. Ophir, I. Ohad, *Plant Cell* **2005**, *17*, 2580.
[34] W. Yang, Y. Yu, M. B. Starr, *Nano Lett.* **2015**, *15*, 7574.
[35] I. S. Cho, C. H. Lee, Y. Feng, *Nat. Commun.* **2013**, *4*, 1723.
[36] W. Zhou, Z. Yin, Y. Du, X. Huang, Z. Zeng, Z. Fan, H. Liu, J. Wang, H. Zhang, *Small* **2013**, *9*, 140.
[37] X. Xia, J. Tu, Y. Zhang, J. Chen, X. Wang, C. Gu, C. Guan, J. Luo, H. J. Fan, *Chem. Mater.* **2012**, *24*, 3793.
[38] C. Tan, H. Zhang, *Nat. Commun.* **2015**, *6*, 7873.
[39] Z. Sun, T. Liao, Y. Dou, *Nat. Commun.* **2014**, *5*, 3813.
[40] X. Feng, K. Shankar, O. K. Varghese, *Nano Lett.* **2008**, *8*, 3781.
[41] Z. Li, S. Feng, S. Liu, X. Li, L. Wang, W. Lu, *Nanoscale* **2015**, *7*, 19178.
[42] S. K. Joung, T. Amemiya, M. Murabayashi, K. Itoh, *Chemistry* **2006**, *12*, 5526.
[43] Y. N. Nuli, Y. Q. Chu, Q. Z. Qin, *J. Electrochem. Soc.* **2004**, *151*, A1077.
[44] R. Zhang, S. He, Y. Lu, W. Chen, *J. Mater. Chem. A* **2015**, *3*, 3559.
[45] Y. Lin, W. Yao, Y. Cheng, *J. Mater. Chem.* **2012**, *22*, 5684.

Received: February 17, 2016
Revised: March 20, 2016
Published online:

DOI: 10.1002/smll.201600534